

# Autonomous AI for Multi-Pathology Detection in Chest X-Rays: A Multi-Site Study in Indian Healthcare System

Bargava Subramanian, Dr. Shajeev Jaikumar, Dr. Praveen Shastry  
Naveen Kumarasami, Kalyan Sivasailam, Anandakumar D  
Keerthana R, Mounigasri M, Kishore Prasath Venkatesh

## Abstract

**Study Design** The study outlines the development of an autonomous AI system for chest X-ray (CXR) interpretation, trained on a vast dataset of over 5 million X-rays sourced from healthcare systems across India. This AI system integrates advanced architectures, including Vision Transformers, Faster R-CNN, and various U-Net models (such as Attention U-Net, U-Net++, and Dense U-Net), to enable comprehensive classification, detection, and segmentation of 75 distinct pathologies. To ensure robustness, the study design includes subgroup analyses across age, gender, and equipment type, validating the model's adaptability and performance across diverse patient demographics and imaging environments.

**Performance** The AI system achieved up to 98% precision and over 95% recall for multi-pathology classification, with stable performance across demographic and equipment subgroups. For normal vs. abnormal classification, it reached 99.8% precision, 99.6% recall, and 99.9% negative predictive value (NPV). Deployed in 17 major healthcare systems in India, including diagnostic centers, large hospitals, and government hospitals. Over the deployment, it processed around 150,000+ scans, averaging 2,000 chest X-rays daily, resulting in reduced reporting times and improved diagnostic accuracy.

**Conclusion** The high precision and recall validate the AI's capability as a reliable tool for autonomous normal/abnormal classification, pathology localization, and segmentation. This scalable AI model addresses diagnostic gaps in underserved areas, optimizing radiology workflows and enhancing patient care across diverse healthcare settings in India.

# Introduction

Chest X-ray (CXR) imaging is an essential diagnostic tool in India, widely used for detecting thoracic diseases, including pneumonia, tuberculosis (TB), lung cancer, and cardiovascular conditions. India bears a significant burden of infectious and respiratory diseases, with TB alone contributing to over a quarter of global cases [1]. Millions of CXRs are conducted annually, creating a substantial demand for radiologists, especially given the limitations of traditional interpretation methods. These methods struggle with high workloads, variability in interpretations, and the risk of missed diagnoses, with studies indicating that up to 30% of abnormalities may go undetected [2]. This underscores the urgent need for enhanced solutions to improve the accuracy and efficiency of CXR analysis.

The healthcare system in India is further strained by a critical shortage of radiologists. With fewer than 15,000 radiologists serving a population of over 1.4 billion, there is an immense gap between demand and supply [3]. This shortage is particularly pronounced in rural areas, which lack adequate access to diagnostic services, leaving a large portion of the population underserved. The growing burden of diseases such as tuberculosis and post-COVID-19 complications further amplifies the need for timely, scalable diagnostic solutions [4]. Addressing these challenges requires a shift towards AI-driven technologies that can alleviate the workload, standardize reporting quality, and provide quicker patient care.

This paper presents an AI-based approach designed to address these challenges in the Indian healthcare system by enhancing CXR pathology detection capabilities. The system is capable of detecting 75 distinct pathologies, from common infections to complex thoracic conditions, using a combination of Vision Transformers for classification, Faster R-CNN for detection, and UNet for segmentation [5]. This multi-layered approach enables precise identification of abnormalities while automating the detection and reporting process. We begin by outlining the challenges in CXR reporting within India and describe how AI is uniquely positioned to tackle these issues [6]. The paper also elaborates on the methodology, covering the system architecture and workflow from input to pathology detection, aimed at providing accurate and actionable insights [7].

The results section highlights the effectiveness of this AI solution, showing precision rates up to 97% and recall exceeding 95%, demonstrating its ability to enhance diagnostic workflows significantly. By reducing reporting times by up to 50%, the AI-driven approach can address the high demand for CXR interpretation in India, thereby improving patient care and clinical outcomes [8]. This integration of AI into clinical workflows offers an opportunity to bridge the diagnostic gap, particularly in underserved areas, supporting healthcare professionals, enhancing diagnostic accuracy, and ultimately contributing to better patient outcomes across India [9].

## Methodology

### AI System Overview

The AI system developed for this study is a computer-aided detection (CAD) tool designed for the identification and differentiation of various radiological abnormalities present in

chest X-rays (CXRs). This system incorporates multiple deep-learning algorithms, each tailored to detect specific pathologies, covering a comprehensive range of thoracic conditions (Ronneberger et al., 2015). The models were trained on a large-scale dataset consisting of over 5 million CXR images, with expert radiologist annotations used for supervised learning (Firdiantika & Jusman, 2022). The AI system aims to detect abnormalities such as lung nodules, pleural effusion, pneumothorax, cardiomegaly, consolidation, fibrosis, hilar enlargement, rib fractures, etc.

Alveolar Lung Opacity	Foreign Body - Intercostal	Nodule
Atelectasis	Foreign Body - Nasogastric Tube	Old Healed Clavicle Fracture
Azygous Lobe	Foreign Body - Nasojejunal Tube	Old Rib Fracture
Bifid Rib	Foreign Body - Pacemaker	Old Tuberculosis
Bronchiectasis	Foreign Body - Pigtail Catheter	Pericardial Cyst
Bullous Emphysema	Foreign Body - Spinal Fusion	Pleural Calcification
Cardiomegaly	Foreign Body - Sternal Sutures	Pleural Effusion
Cavity	Foreign Body - Tracheostomy Tube	Pleural Plaque
Cervical Rib	Hilar Lymphadenopathy	Pleural Thickening
Clavicle Fracture	Hilar Prominence	Pneumonia
Clavicle Fracture with PO	Humerus Fracture	Pneumoperitoneum
Consolidation	Humerus Post OP	Pneumothorax
Dextrocardia	Hydro Pneumothorax	Prominent Bronchovascular Markings
Dextrocardia with situs inversus	Hypoplastic Rib	Pulmonary Edema
Diaphragmatic Hump	Interstitial Lung Disease	Reticulo-nodular Appearance
Elevated Diaphragm	Interstitial Lung Opacity	Rib Fracture
Esophageal Stent	Lobe Collapse	Scapula Fracture
Fibrosis	Lung Collapse	Scoliosis
Fissural Thickening	Lung Mass	Subcutaneous Emphysema
Flattened Diaphragm	Lymph Node Calcification	Surgical Staples
Foreign Body - Cardiac Valves	Mastectomy	Thyroid Lesion
Foreign Body - Chemoport	Mediastinal Mass	Tracheal and Mediastinal Shift
Foreign Body - Chest Leads	Mediastinal Shift	Tracheal Shift
Foreign Body - CV Line	Mediastinal Widening	Tuberculosis
Foreign Body - Endotracheal tube	Milliary Tuberculosis	Unfolding of Aorta

Table 1: List of 75 Pathologies

The detection system employs a stepwise approach to analyze CXRs, focusing on both the identification of specific abnormalities and the overall classification of findings. Initially,

the system processes the input image to classify it as whether it’s a valid CXR or not. Following this initial classification, the model performs detailed detection to identify and localize specific pathologies within the CXR, such as lung nodules, pleural effusion, pneumothorax, and other abnormalities [12].

In this study, the primary focus was on the comprehensive detection of various pathologies present in each CXR, rather than just distinguishing between normal and abnormal [13]. By doing so, the system enables a more thorough analysis of each radiograph, providing granular details about identified pathologies. This focus on detailed detection enhances the accuracy of the diagnostic process and aids radiologists in making informed decisions, ultimately contributing to better patient outcomes [14].

## Dataset

This study utilized a dataset of 5,003,742 chest X-ray (CXR) scans gathered from various healthcare facilities. The dataset was split into three subsets: Training, Live Clinical Trial, and Live Clinical Deployment, with slightly varied proportions to support model development, validation, and real-world application.

Training Set: 3,997,891 scans  
 Live Clinical Trial: 855,482 scans  
 Live Clinical Deployment: 157,369 scans

## Age Group Distribution

Scans were distributed across age groups to capture demographic diversity:

Age Group	Total Scans	Training Set	Live Clinical Trial	Live Clinical Deployment
Under 18	691,487	600,208	75,732	15,547
18-40	1,779,807	1,404,071	327,429	48,307
40-60	1,424,936	1,201,381	189,765	33,790
60-75	1,187,200	1,004,752	151,034	31,414
75+	933,312	793,479	111,522	28,311

Table 2: Scans distribution based on Age Group

## Gender Distribution

The dataset maintained a balanced gender distribution:

<b>Gender</b>	<b>Total Scans</b>	<b>Training Set</b>	<b>Live Clinical Trial</b>	<b>Live Clinical Deployment</b>
Male	3,338,809	2,799,453	453,688	85,668
Female	2,677,933	2,204,438	401,794	71,701

Table 3: Scans distribution based on Gender

## Manufacturer Type Distribution

Scans were categorized by equipment manufacturer to account for variability in imaging conditions:

<b>Manufacturer</b>	<b>Total Scans</b>	<b>Training Set</b>	<b>Live Clinical Trial</b>	<b>Live Clinical Deployment</b>
GE Healthcare	1,866,094	1,549,878	263,487	52,729
Siemens	1,423,256	1,152,414	230,532	40,310
Philips	1,395,340	1,158,413	203,287	33,640
Other Manufacturers	1,332,052	1,143,186	158,176	30,690

Table 4: Scans distribution based on Manufacturer Type

## Equipment Type Distribution

Scans were categorized by equipment type to account for variability in imaging conditions:

<b>Machine Type</b>	<b>Total Scans</b>	<b>Training Set</b>	<b>Live Clinical Trial</b>	<b>Live Clinical Deployment</b>
CR	4,153,207	3,502,723	556,063	94,421
DR	1,863,535	1,501,168	299,419	62,948

Table 5: Scans by Machine Type

This dataset composition, with varied proportions across training, trial, and deployment, ensures comprehensive model training, rigorous validation in clinical trials, and real-world testing, supporting reliable application across diverse demographics and equipment settings in clinical workflows. To maintain compliance with ethical guidelines and data protection

standards, all patient data underwent rigorous anonymization, ensuring complete privacy by removing identifiable patient information before use in this study, in compliance with HIPAA.

## **Distinct Quality Challenges in Indian CXR Datasets**

In the context of India, there are unique challenges that significantly impact the quality and diagnostic accuracy of CXR imaging. These include rotations, artifacts, suboptimal images, etc.. Rotational issues in images may result from improper patient positioning, while artifacts can be introduced due to equipment limitations or external objects during imaging. Suboptimal images, often a result of inadequate imaging conditions or limited resources in some facilities, can lead to difficulties in detecting pathologies accurately. To address these challenges, the dataset included a diverse range of CXR images, spanning from below-average quality to high-quality images. This range allowed the AI model to be trained on various levels of image quality, making it more robust and capable of handling live clinical diagnosis scenarios where image quality may vary significantly. By incorporating these lower-quality images into training, the model becomes better equipped to identify abnormalities effectively across different imaging conditions, enhancing its utility in both urban and rural healthcare settings in India.

## **Architecture**

The architecture of the system is divided into multiple phases, including the Annotation Phase, Analysis and Detection Phase. Each of these phases plays a critical role in ensuring accurate and efficient detection of pathologies in chest X-rays (CXR). Below is a detailed explanation of each phase:

### **Annotation Phase**

#### **Dataset Segregation**

The annotation process forms the foundational step of the overall workflow. It begins by segregating chest radiograph images into unlabelled and labeled datasets [15]. This data is further categorized into Posterior-Anterior (PA) views and Anterior-Posterior (AP) views to provide distinct training inputs, as these views are critical for detecting pathologies accurately [16]. The annotation phase involves handling both labeled and unlabelled data to ensure a comprehensive and diverse dataset that can enhance model generalizability [17].

#### **Dataset Selection**

After the dataset segregation, the images proceed to dataset selection, where the appropriate subset of data is chosen based on the requirements of the training task [18]. This careful selection helps ensure that only relevant images are processed, which subsequently improves the performance of downstream tasks [19].

## Dataset Pre-processing

Once the dataset is selected, the next step is pre-processing. Pre-processing involves adjusting image quality, size, and other properties to maintain uniformity across the dataset [20]. This consistency in image quality is essential for the model to extract relevant features efficiently and ensures that the CXR images are well-prepared for further analysis [21]. This process also plays a role in minimizing noise and enhancing the clarity of key anatomical features [22].

## Cross Teaching

To further leverage the unlabelled data, the cross-teaching phase is applied. Cross-teaching is a semi-supervised learning approach where multiple models iteratively train each other using both labeled and unlabelled data, enhancing generalization and robustness [23]. By integrating labeled and unlabelled data during the learning phase, the system is capable of utilizing a more extensive dataset, ultimately improving detection performance [24].

## Training Phase

The training phase begins with preprocessing and initial classification steps that prepare each image for detailed pathology detection. The input chest X-ray images, originally in DICOM format, are converted to JPEG using *pydicom* for compatibility with deep-learning models. The architecture is designed to handle high variability in imaging quality by incorporating a multi-resolution analysis approach, enabling the model to capture a range of details essential for accurate classification and detection.

## Initial Classification and Preliminary Verification with Vision Transformers

Each image enters the training pipeline through a Vision Transformer (ViT) model, where initial classifications and sanity checks are performed. These checks include:

- **Image Verification:** The model verifies if the image is an X-ray, filtering out non-X-ray images..
- **Chest X-Ray Identification:** The next classification confirms if the X-ray is specifically a chest X-ray, distinguishing it from other anatomical regions (e.g., extremities, abdomen).
- **View Classification:** The model first analyzes the chest X-ray to classify it as either Posterior-Anterior (PA) or Anterior-Posterior (AP), ensuring accurate interpretation. This classification is essential as PA and AP views differ in anatomical perspective, impacting pathology detection.
- **Rotation Correction with Keypoint Detection:** The model detects specific anatomical landmarks, such as the clavicles and spinous process, to correct any rotational misalignment in the X-ray. By aligning these key points—especially focusing on the



relative positions of the clavicles and spinous process—the model can accurately compute and apply the necessary rotation adjustments, ensuring that all images have a consistent, upright orientation.

## Normal and Abnormal Classification with Multi-Resolution Analysis

Following the sanity checks, each radiograph is classified as normal or abnormal using a Vision Transformer. In this phase, multi-resolution analysis is a critical component of training, allowing the model to analyze images at different pixel resolutions to capture features across varying levels of detail:

- **224x224 pixels:** This lower resolution provides a broader view of the structure, suitable for identifying larger abnormalities and general patterns within the chest X-ray.
- **320x320 pixels:** At this intermediate resolution, the model gains access to finer details, making it more sensitive to subtle features that may not be visible at lower resolutions.
- **512x512 pixels:** This higher resolution is used to capture intricate details and small abnormalities, essential for detecting minor pathologies or subtle changes within the image.

## Output Layer Structuring

At the final layer of the Vision Transformer used for normal vs. abnormal classification, a 2-class softmax output layer is used. This layer focuses on the binary labels: **Normal** and **Abnormal**. This simplified output reduces complexity at the classification step, ensuring that the model remains focused on the essential diagnostic categories.

Each resolution is trained separately on the dataset, and the model predictions from each resolution are then combined using an ensemble averaging technique. This ensemble approach integrates predictions from all three resolutions, enhancing the robustness and accuracy of the normal/abnormal classification. This ensemble approach leverages the unique spatial and structural information captured at each resolution, effectively balancing the detection of both large-scale anomalies and fine-grained pathological features.

This multi-resolution training strategy significantly enhances the Vision Transformer’s ability to distinguish between normal and abnormal cases, supporting more accurate downstream pathology detection and segmentation.

## Analysis and Detection Phase

In the analysis and detection phase, abnormal images are processed through a specialized model stack optimized for comprehensive pathology identification and segmentation. This stack includes a Faster R-CNN for detecting pathology locations and a family of U-Net architectures (Attention U-Net, U-Net++, Dense U-Net) for high-precision segmentation.

## Pathology Detection with Faster R-CNN

The Faster R-CNN model detects and localizes abnormalities by generating bounding boxes around potential pathology regions. Key parameter configurations include:

- **Anchor Boxes:** Configured with sizes of 128, 256, and 512 pixels and aspect ratios of 1:1, 2:1, and 1:2 to cover a wide range of pathology sizes.
- **Region Proposal Network (RPN):**
  - **NMS Threshold:** 0.7 to eliminate highly overlapping proposals.
  - **Top Proposals:** 2,000 per image during training and 300 during inference for optimal computational efficiency.
- **Bounding Box Regression:**
  - **Smooth L1 Loss** with  $\beta = 1.0$  to handle localization adjustments without being overly sensitive to small shifts.
  - **Bounding Box  $\Delta$  Parameters:** Set to  $\Delta_x = \Delta_y = 0.1$  and  $\Delta_w = \Delta_h = 0.2$  to adjust bounding box predictions for chest X-ray anatomy.

## Segmentation with the U-Net Family (Attention U-Net, U-Net++, Dense U-Net)

After bounding box localization, each abnormal region is further segmented using a combination of U-Net variants, specifically Attention U-Net, U-Net++, and Dense U-Net. These architectures are chosen for their unique capabilities to improve segmentation accuracy in complex medical images.

**1. Attention U-Net** The Attention U-Net model enhances the base U-Net with attention gates that focus on relevant regions, suppressing irrelevant background features. Key configurations include:

- **Attention Gate Parameters:**
  - **Gate Activation:** Sigmoid with a threshold of 0.5 to selectively highlight pathology-relevant regions.
  - **Inter-Channel Weighting:** Emphasizes pathological features by learning spatially adaptive weights, useful in suppressing noise from surrounding anatomical structures.
- **Encoder-Decoder Structure:** Depth of five levels, with initial filter size of 64, doubling at each level (64, 128, 256, 512, 1024).

**2. U-Net++** U-Net++ improves segmentation precision by utilizing densely connected skip pathways and redesigned skip connections, allowing more detailed information transfer between the encoder and decoder.

- **Nested Architecture:** Employs dense skip connections across intermediate layers, allowing the network to learn fine-grained details that enhance segmentation accuracy for complex pathologies.
- **Filter Sizes and Depth:** Five levels, with a base filter size of 64, increasing at each level.

**3. Dense U-Net** The Dense U-Net model leverages densely connected layers within the encoder and decoder, enabling feature reuse and better gradient flow, which is particularly useful for handling images with high variability in pathological regions.

- **Dense Connections:** Each layer within the encoder and decoder receives input from all preceding layers, preserving features across all stages and improving the model's ability to capture details in complex structures.
- **Filter Configuration:** Initial filter size of 32, with four dense blocks, each with growth rate  $k = 12$  to control the number of features per layer.

### Training and Inference Parameters for the U-Net Family

- **Batch Size:** Set to 8 for efficient memory usage while maintaining stable gradients.
- **Learning Rate:** 0.0005 with decay factor 0.9, adjusting every 15 epochs.
- **Dropout Rate:** 0.3 applied in each decoder block to prevent overfitting, given the variability in chest X-ray images.
- **Post-Processing Threshold:** Softmax threshold set at 0.5 across all U-Net outputs to retain high-probability regions as pathologies.

### End-to-End Workflow

- **Input Validation and Preliminary Verification:** JPEG-formatted DICOM images undergo validation for modality, chest X-ray type, view identification, and rotation correction.
- **Normal/Abnormal Classification with Multi-Resolution Analysis:** A Vision Transformer classifies images at multiple resolutions (224x224, 320x320, and 512x512), followed by ensemble averaging for final output.
- **Pathology Detection:** Faster R-CNN generates bounding boxes for each detected pathology.

- **Segmentation by U-Net Family:** The Attention U-Net, U-Net++, and Dense U-Net models process each region to produce pixel-level segmentations, enhancing interpretability with high spatial accuracy.

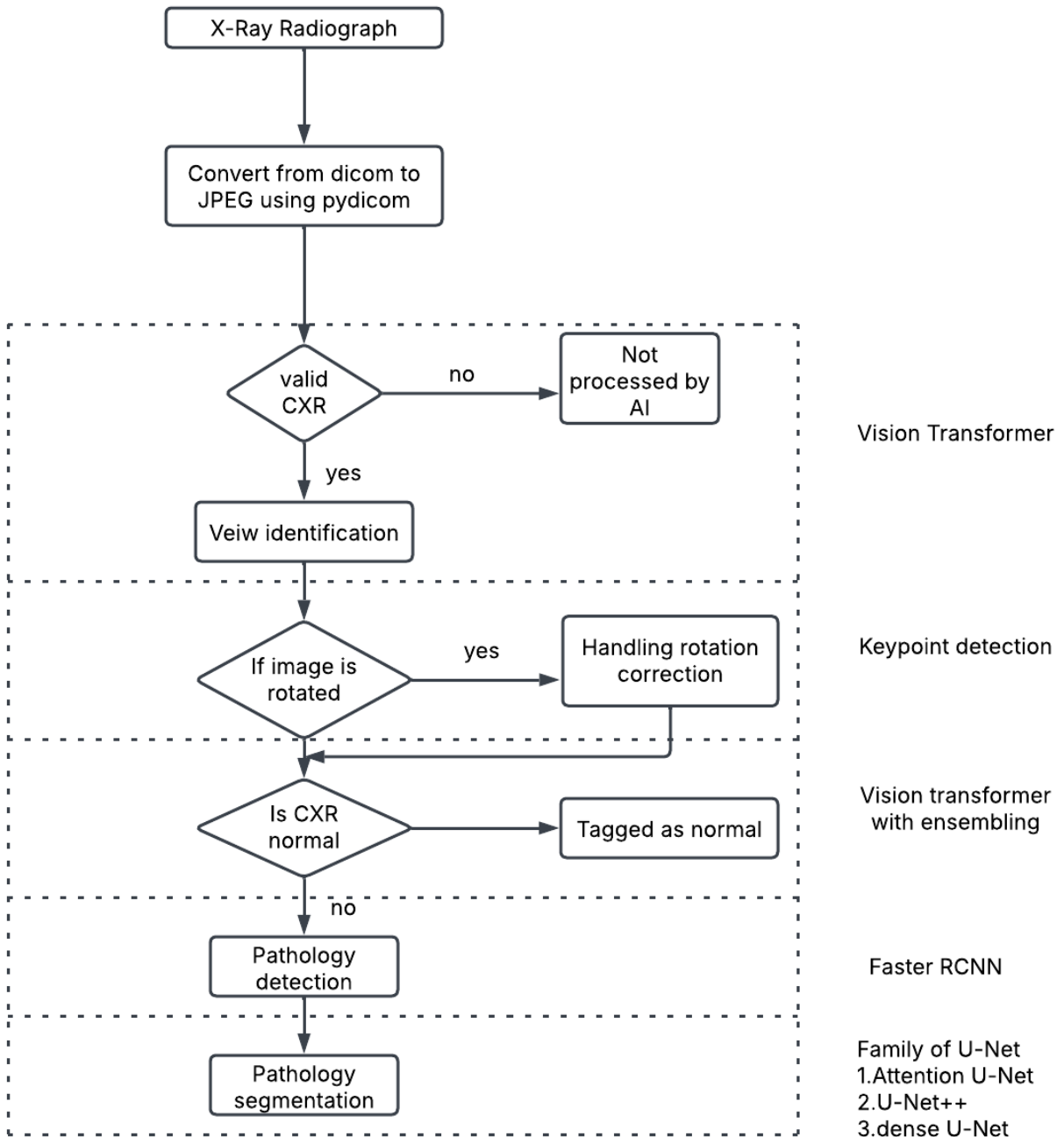


Figure 1: Workflow Architecture

## Evaluation Metrics:

The performance of the chest X-ray analysis system was evaluated comprehensively using a set of metrics for both classification and detection tasks to understand its effectiveness in real clinical environments. For the classification component, we used Negative Predictive Value (NPV) and Positive Predictive Value (PPV) to gauge the model’s accuracy in classifying chest X-rays as normal or abnormal. The Positive Percent Agreement (PPA) and Negative Percent Agreement (NPA) metrics were also calculated to determine how well the model’s predictions aligned with radiologists’ evaluations. These metrics, along with the associated 95% confidence intervals, provide a robust measure of the system’s accuracy and reliability in distinguishing between normal and abnormal cases.

Moving beyond classification, the detection capability of the model was evaluated using Precision, Recall, and Intersection over Union(IoU) metrics. Precision indicates how many of the abnormalities identified by the model were true positives, while recall measures the ability of the model to identify all existing abnormalities in the chest X-rays. IoU was utilized to evaluate the overlap between predicted regions of interest and the actual ground truth, offering a quantitative assessment of the model’s localization accuracy. Performance metrics for all 75 detected pathologies were documented, providing an in-depth view of how well the system performed for each specific condition. The metrics for precision, recall for each of these pathologies are presented in the table below, showcasing the AI’s proficiency in both identifying and accurately localizing abnormalities. These results highlight the system’s ability to support clinical workflows, enhancing both the accuracy and speed of radiology reporting.

In general, the combination of classification and detection metrics provides a complete picture of the performance of the model, illustrating its potential to serve as a reliable support tool for radiologists in everyday clinical practice.

Pathology	AUC	Precision (%)	Recall (%)
Alveolar Lung Opacity	0.97	97.40	95.80
Atelectasis	0.98	99.40	97.40
Azygous Lobe	0.99	99.31	99.29
Bifid Rib	0.99	95.79	94.20
Bronchiectasis	0.97	98.60	98.50
Bullous Emphysema	0.97	98.09	95.22
Cardiomegaly	0.96	96.50	95.90
Cavity	0.98	98.09	97.80
Cervical Rib	0.95	95.60	95.00
Clavicle Fracture	0.97	96.90	95.22
Clavicle Fracture with PO	0.98	96.90	99.40
Consolidation	0.96	98.09	94.20
Dextrocardia	0.98	97.00	98.30
Dextrocardia with situs inversus	0.99	98.40	93.00

*Continued on next page*

<b>Pathology</b>	<b>AUC</b>	<b>Precision (%)</b>	<b>Recall (%)</b>
Diaphragmatic Hump	0.97	97.40	96.80
Elevated Diaphragm	0.98	95.70	100.00
Esophageal Stent	0.96	98.00	99.30
Fibrosis	0.99	98.00	99.30
Fissural Thickening	0.98	98.48	98.00
Flattened Diaphragm	0.99	99.31	100.00
Foreign Body - Cardiac Valves	0.99	99.31	99.29
Foreign Body - Chemoport	0.97	97.90	95.40
Foreign Body - Chest Leads	0.98	98.60	97.80
Foreign Body - CV Line	0.97	98.09	95.22
Foreign Body - ETT	0.98	98.73	96.59
Foreign Body - ICD	0.95	95.70	95.10
Foreign Body - Nasojejun Tube	0.95	99.31	99.29
Foreign Body - NG Tube	0.96	96.30	95.90
Foreign Body - Pacemaker	0.98	98.48	98.50
Foreign Body - Pigtail Catheter	0.97	98.40	95.70
Foreign Body - Spinal Fusion	1.00	100.00	99.70
Foreign Body - Sternal Sutures	1.00	100.00	99.80
Foreign Body - Tracheostomy Tube	0.96	95.70	97.00
Hilar Lymphadenopathy	0.99	98.50	95.00
Hilar Prominence	0.98	99.31	99.29
Humerus Fracture	0.99	99.31	98.00
Humerus Post OP	0.97	98.25	96.50
Hydro Pneumothorax	0.99	98.40	97.40
Hypoplastic Rib	0.99	97.80	94.70
Interstitial Lung Disease	0.98	99.31	99.29
Interstitial Lung Opacity	0.98	98.60	97.80
Lobe Collapse	0.96	96.00	95.80
Lung Collapse	0.97	97.60	95.90
Lung Mass	0.97	97.40	96.50
Lymph Node Calcification	0.98	97.80	96.00
Mastectomy	0.97	98.60	97.80
Mediastinal Mass	0.96	95.90	95.00
Mediastinal Shift	0.97	98.10	96.90
Mediastinal Widening	0.98	98.09	95.22
Milliary Tuberculosis	0.98	98.70	95.22
Nodule	1.00	98.48	100.00
Old Healed Clavicle Fracture	0.98	98.30	97.50
Old Rib Fracture	0.98	100.00	100.00
Old TB	0.99	98.48	97.00

*Continued on next page*

<b>Pathology</b>	<b>AUC</b>	<b>Precision (%)</b>	<b>Recall (%)</b>
Pericardial Cyst	0.95	96.70	95.80
Pleural Calcification	0.99	99.30	97.30
Pleural Effusion	0.97	97.30	96.50
Pleural Plaque	0.99	99.20	98.50
Pleural Thickening	0.96	96.80	95.40
Pneumonia	0.97	98.09	97.80
Pneumoperitoneum	0.98	98.73	96.59
Pneumothorax	0.95	95.79	95.20
Prominent Bronchovascular Markings	0.98	98.60	97.80
Pulmonary Edema	0.95	96.50	94.00
Reticulo-nodular Appearance	0.97	99.20	97.60
Rib Fracture	0.98	98.20	97.60
Scapula Fracture	0.96	98.50	96.30
Scoliosis	0.98	97.30	96.40
Subcutaneous Emphysema	0.99	98.00	99.30
Surgical Staples	0.99	95.79	94.20
Thyroid Lesion	0.97	96.90	99.40
Tracheal and Mediastinal Shift	0.97	95.79	96.00
Tracheal Shift	0.98	96.90	99.40
Tuberculosis	0.97	97.60	100.00
Unfolding of aorta	0.98	98.60	99.29

Table 6: Performance Metrics for Detected Pathologies

## ROC Curve Analysis

AUC = 0.9925

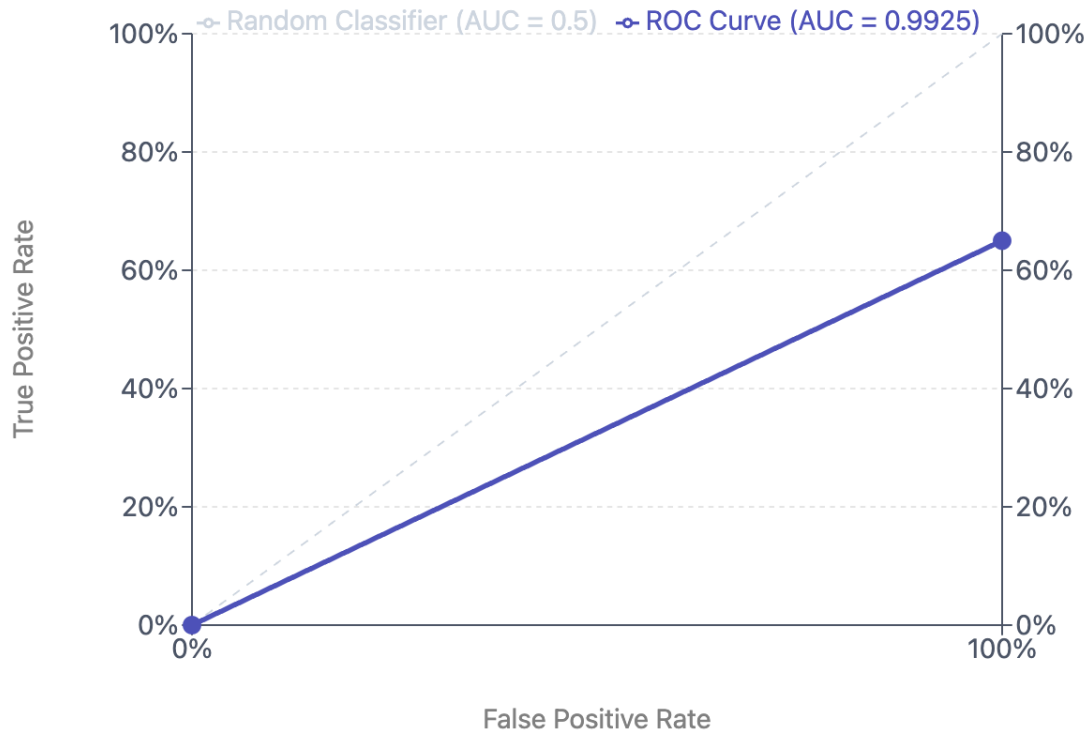
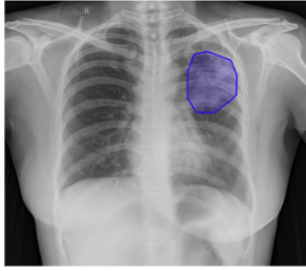
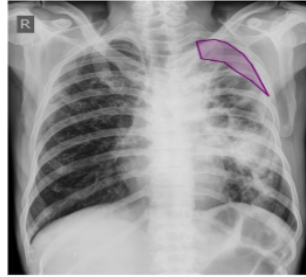


Figure 2: AUC Curve for Normal/Abnormal Classifier

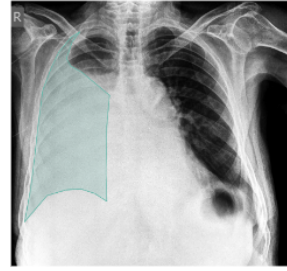




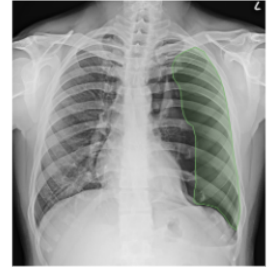
Consolidation



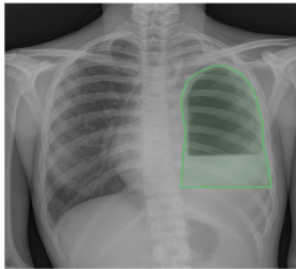
Pleural Thickening



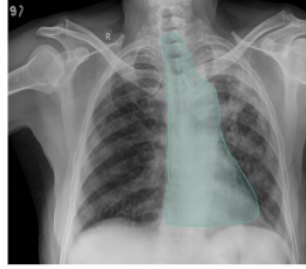
Pleural Effusion



Pneumothorax



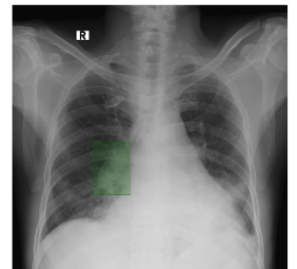
Hydropneumothorax



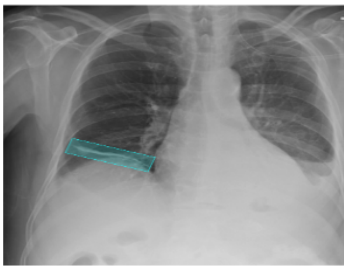
Mediastinal shift



Tracheal shift



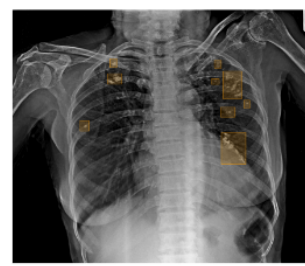
Hilar prominence



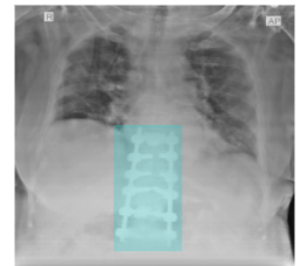
Linear atelectasis



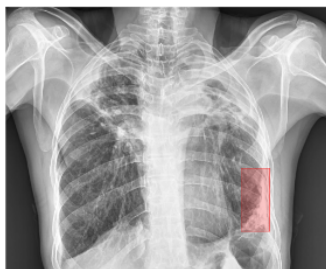
Nodules



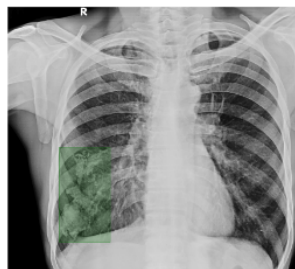
Calcified nodules



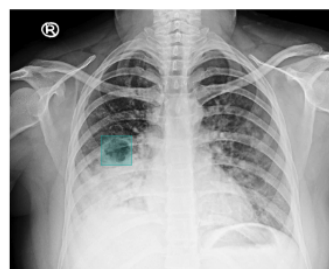
Spinal Fusion



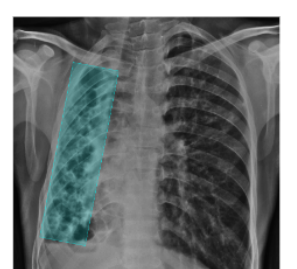
Pleural Calcification



Pleural Plaque



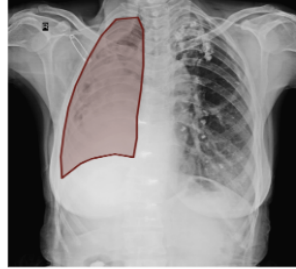
Cavity



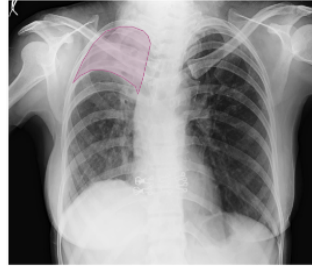
Bronchiectasis



Subcutaneous emphysema



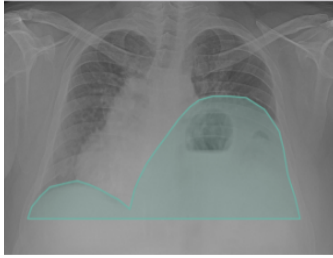
Lung Collapse



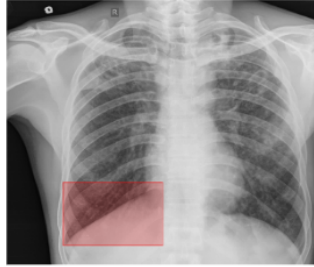
Lobe Collapse



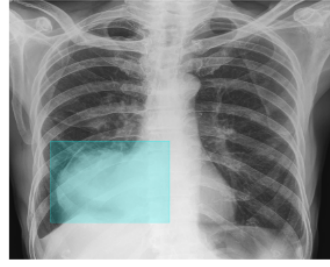
Tented Diaphragm



Elevated Diaphragm



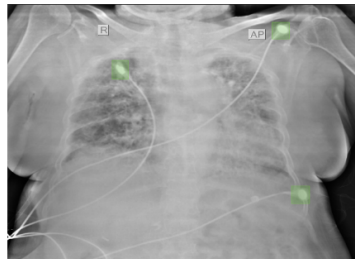
Flattened Diaphragm



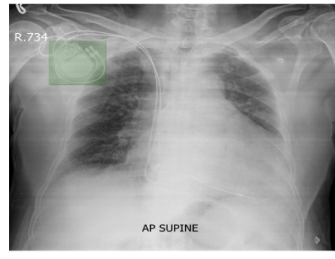
Mediastinal mass



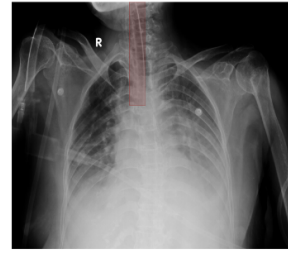
Humerus postoperative



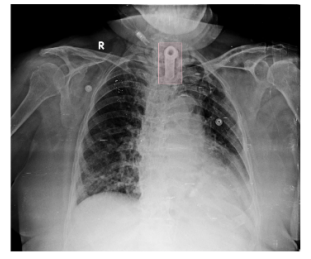
Foreign Body - Chest Leads



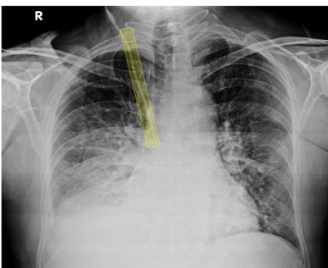
Foreign Body - Pacemaker



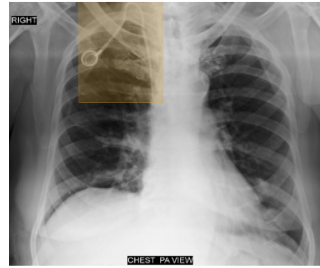
Foreign Body - ET Tube



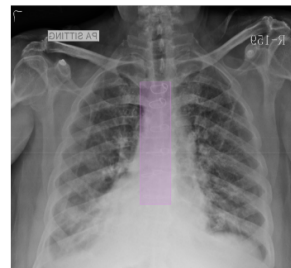
Foreign Body - Tracheostomy Tube



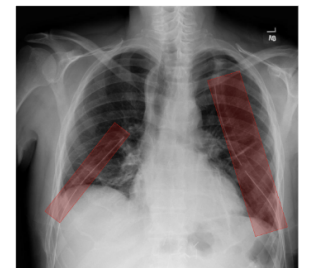
Foreign Body - CV line



Foreign Body - Chemoport



Foreign Body - Sternal sutures



Foreign Body - ICD

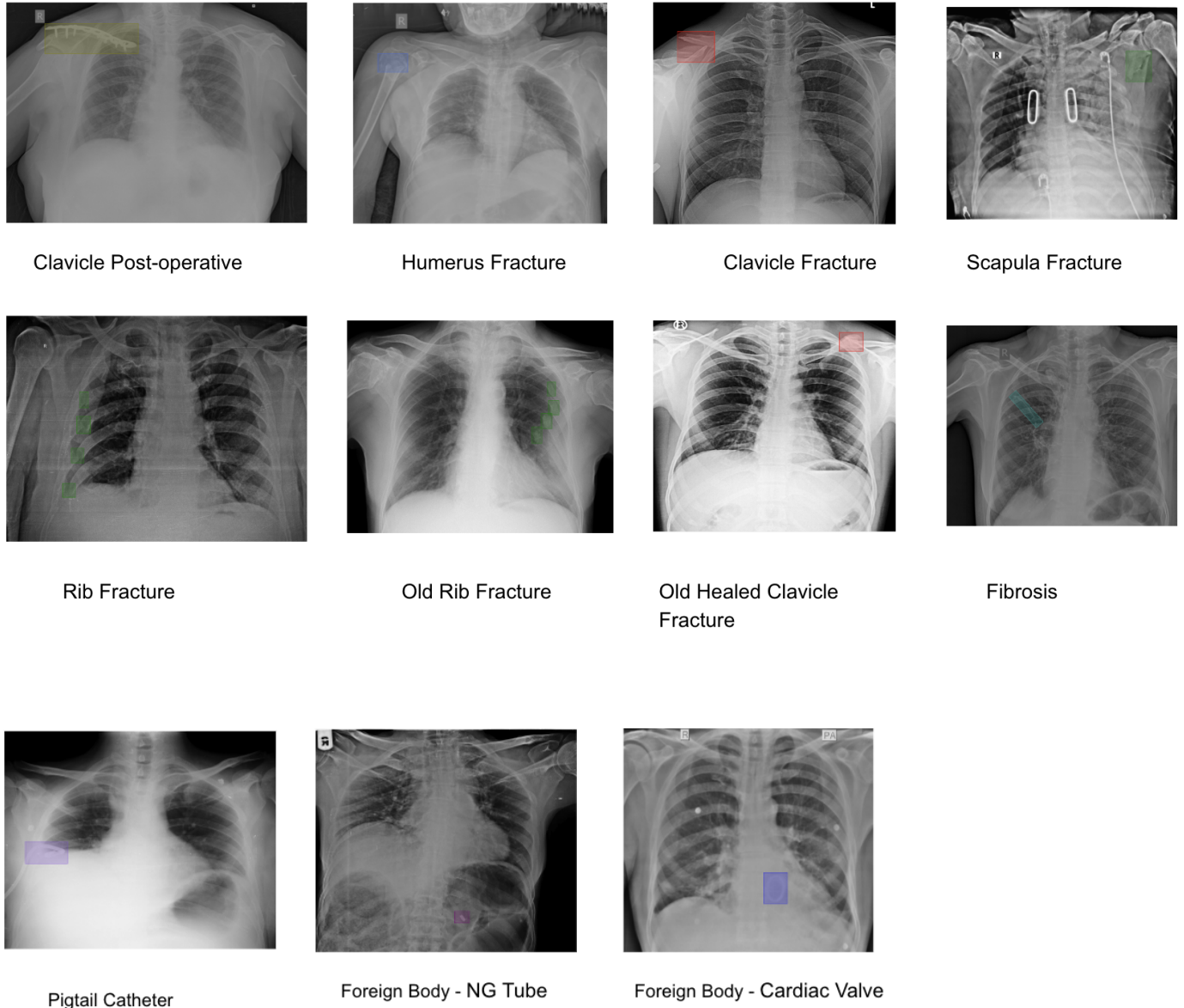


Figure 3: Pathology Detections

## Multi-Site Clinical Trial and Dataset Composition

This study was conducted as a multi-site clinical trial across healthcare facilities in India, encompassing Government hospitals, Large Private Enterprise Hospitals (including 17 Large Enterprise healthcare entities in India), and Small to medium-sized (SME) hospitals. The trial included a dataset of over 1 million chest X-ray scans collected from these sites, providing a robust and diverse sample for model evaluation. This dataset allowed for testing under a wide range of imaging conditions, from high-resolution scans in well-resourced private hospitals to lower-quality images often encountered in government and SME settings. The trial aimed to assess the model's diagnostic accuracy, consistency, and reliability across

diverse imaging environments. Each scan was processed through the model’s classification and detection phases, allowing us to capture detailed performance metrics such as sensitivity, specificity, precision, and recall. The multi-site setup enabled cross-validation across varying levels of image quality, patient demographics, and clinical workflows, ensuring that the model could generalize effectively. By evaluating performance across 1 million scans in different healthcare settings, this study provided a rigorous assessment of the model’s applicability and scalability for widespread deployment within the Indian healthcare system.

## Subgroup Analysis

Subgroup analysis is essential to assess the model’s generalizability across diverse clinical conditions and demographics. By evaluating performance across age, X-ray machine manufacturer, and gender, we ensure that the model can handle anatomical differences, equipment variability, and demographic diversity without bias. This approach verifies that the model maintains consistent accuracy, precision, and recall across real-world scenarios, making it reliable and adaptable for deployment across varied healthcare settings.

The results for accuracy, precision, recall, sensitivity, and specificity across these subgroups are presented in the table below:

Age Group	AUC	Accuracy (%)	Precision (%)	Recall (%)	Sensitivity (%)	Specificity (%)
Under 18	0.903	96.5	96.2	96.8	96.5	97.0
18-40	0.986	98.2	98.0	98.3	98.0	98.5
40-60	0.972	97.8	97.5	98.0	97.8	98.3
60-75	0.976	97.2	96.3	96.8	97.0	98.1
75+	0.885	95.3	94.8	95.0	96.3	96.9

Table 7: Performance Metrics by Age Group

Gender	AUC	Accuracy (%)	Precision (%)	Recall (%)	Sensitivity (%)	Specificity (%)
Male	0.986	98.0	97.9	98.1	98.0	98.2
Female	0.979	97.8	97.6	98.1	97.8	98.0

Table 8: Performance Metrics by Gender

Machine Type	AUC	Accuracy (%)	Precision (%)	Recall (%)	Sensitivity (%)	Specificity (%)
CR	0.978	98.2	97.4	98.3	97.6	97.9
DR	0.969	97.5	96.9	97.5	97.1	98.0

Table 9: Performance Metrics by Machine Type

Manufacturer	AUC	Accuracy (%)	Precision (%)	Recall (%)	Sensitivity (%)	Specificity (%)
GE Healthcare	0.95	98.1	97.8	98.3	98.0	97.5
Siemens	0.967	97.9	97.6	98.1	97.7	98.0
Philips	0.921	98.0	97.9	98.2	97.8	98.3
Other Manufacturers	0.934	97.5	97.3	97.8	97.6	97.7

Table 10: Performance Metrics by Manufacturer

## Deployment at live Radiology Reporting Workflow:

The AI software has been deployed across 17 major healthcare systems in India, covering both urban and rural settings. Integrated into 5C Network’s clinical workflows, the AI system has processed over 157,369 chest X-rays, averaging around 2,000+ CXR scans per day. The system performs automated classification of chest X-rays into normal and abnormal categories and detects specific pathologies, enabling rapid identification and triage of scans. This setup reduces time spent on routine cases, allowing radiologists to focus on critical findings like pneumothorax, which require prompt intervention.

## Radiologist Validation of AI Predictions:

After the AI processes a scan, its predictions are presented to the radiologists for review. Radiologists assess the AI-generated findings, validating or rejecting each classification and annotation. This feedback mechanism allows radiologists to indicate which predictions are accurate and identify any discrepancies, providing direct input on the model’s performance. Each accepted or rejected prediction is logged, enabling continuous refinement of the AI model based on radiologists’ expertise and feedback. This validation loop ensures that the AI adapts to clinical requirements and maintains high predictive accuracy.

## Post-deployment Results:

Pathology	AUC	Precision (%)	Recall (%)
Alveolar Lung Opacity	0.96	96.90	96.08
Atelectasis	0.99	98.11	97.75
Azygous Lobe	0.99	99.03	99.64
Bifid Rib	0.99	96.22	93.70
Bronchiectasis	0.98	99.12	98.88
Bullous Emphysema	0.97	98.52	94.83
Cardiomegaly	0.96	96.85	95.40
Cavity	0.97	98.10	97.40

*Continued on next page*

<b>Pathology</b>	<b>AUC</b>	<b>Precision (%)</b>	<b>Recall (%)</b>
Cervical Rib	0.96	96.00	95.43
Clavicle Fracture	0.98	98.52	95.50
Clavicle Fracture with PO	0.98	97.30	98.90
Consolidation	0.97	96.17	93.81
Dextrocardia	0.98	97.38	98.65
Dextrocardia with situs inversus	0.99	98.78	92.50
Diaphragmatic Hump	0.97	97.75	97.23
Elevated Diaphragm	0.97	95.42	99.60
Esophageal Stent	0.97	97.50	98.90
Fibrosis	0.99	97.61	99.73
Fissural Thickening	0.98	98.88	97.80
Flattened Diaphragm	0.99	98.20	100.38
Foreign Body - Cardiac Valves	1.00	99.71	99.69
Foreign Body - Chemoport	0.97	98.33	95.00
Foreign Body - Chest Leads	0.99	98.95	98.15
Foreign Body - CV Line	0.97	98.47	95.60
Foreign Body - ETT	0.98	99.13	96.99
Foreign Body - ICD	0.96	95.98	95.38
Foreign Body - Nasojejunal Tube	0.95	98.92	99.72
Foreign Body - NG Tube	0.96	95.80	95.40
Foreign Body - Pacemaker	0.99	98.91	98.93
Foreign Body - Pigtail Catheter	0.97	98.01	96.10
Foreign Body - Spinal Fusion	1.00	100.00	99.50
Foreign Body - Sternal Sutures	1.00	100.00	99.40
Foreign Body - Tracheostomy Tube	0.97	96.10	97.40
Hilar Lymphadenopathy	0.98	98.23	94.60
Hilar Prominence	0.99	98.81	98.89
Humerus Fracture	0.99	98.92	98.35
Humerus Post OP	0.98	98.65	96.88
Hydro Pneumothorax	0.99	98.01	97.83
Hypoplastic Rib	0.99	98.23	95.10
ILD	0.98	99.03	99.64
Interstitial Lung Opacity	0.98	98.10	98.18
Lobe Collapse	0.96	96.35	96.20
Lung Collapse	0.97	97.98	96.18
Lung Mass	0.97	97.75	96.85
Lymph Node Calcification	0.96	97.70	95.72
Mastectomy	0.97	99.03	98.20
Mediastinal Mass	0.96	96.25	95.28
Mediastinal Shift	0.97	97.60	96.70

*Continued on next page*

Pathology	AUC	Precision (%)	Recall (%)
Mediastinal Widening	0.98	98.49	95.57
Milliary Tuberculosis	0.98	98.49	94.72
Nodule	1.00	98.83	99.72
Old Healed Clavicle Fracture	0.98	98.68	97.88
Old Rib Fracture	0.98	100.38	99.50
Old TB	1.00	99.05	97.43
Pericardial Cyst	0.96	97.10	95.40
Pleural Calcification	0.99	99.70	96.91
Pleural Effusion	0.96	96.80	96.00
Pleural Plaque	0.98	98.81	98.11
Pleural Thickening	0.96	96.52	95.12
Pneumonia	0.97	99.03	97.52
Pneumoperitoneum	0.98	98.34	96.31
Pneumothorax	0.96	96.22	95.63
Prominent Bronchovascular Markings	0.98	98.10	98.18
Pulmonary Edema	0.95	96.11	94.38
Reticulo-nodular Appearance	0.97	98.92	97.10
Rib Fracture	0.98	97.92	98.03
Scapula Fracture	0.96	98.90	96.65
Scoliosis	0.98	96.80	96.83
Subcutaneous Emphysema	0.99	98.40	99.70
Surgical Staples	0.98	95.51	94.00
Thyroid Lesion	0.97	97.33	99.00
Tracheal and Mediastinal Shift	0.95	97.95	96.38
Tracheal Shift	0.98	96.51	98.90
Tuberculosis	0.97	98.88	100.35
Unfolding of aorta	0.98	98.81	98.90

Table 11: Performance Metrics for Detected Pathologies

## Limitations and Considerations

Our AI model, while demonstrating substantial advancements in multi-pathology detection for chest X-rays, is subject to certain limitations and considerations:

- **Complexity in Pathology Segmentation:** Accurately segmenting overlapping structures or low-contrast areas, such as dense lung regions, can be challenging, potentially affecting segmentation precision.
- **Dependence on Image Preprocessing:** The model’s accuracy relies on consistent preprocessing steps, and deviations in techniques, such as rotation correction or contrast adjustments, may affect detection performance.

- **Population-Specific Adaptability:** With training data largely sourced from Indian healthcare systems, the model’s generalizability to other populations or regions might be limited.

## Conclusion

This study demonstrates the efficacy of an autonomous AI system for multi-pathology detection in chest X-rays, addressing critical diagnostic gaps in the Indian healthcare landscape. By leveraging advanced deep-learning architectures such as Vision Transformers, Faster R-CNN, and U-Net variants, the system achieved high precision and recall across 75 pathologies, validated on over 5 million CXRs and deployed across 17 major healthcare institutions. Notably, its integration into clinical workflows has reduced radiology reporting times by up to 50%, significantly improving efficiency while maintaining diagnostic accuracy. This reduction is particularly impactful in addressing the high demand for radiology services, enabling faster decision-making and better patient care, especially in underserved regions where radiologist shortages persist. The AI-driven approach offers a scalable, cost-effective solution that ensures consistent, high-quality interpretations, enhancing overall healthcare outcomes. Looking ahead, further advancements will focus on expanding pathology coverage, improving AI-assisted clinical decision support, and optimizing deployment in resource-limited settings. Additionally, broader multi-site validation beyond India will be essential for ensuring global applicability. As AI continues to evolve, its role in radiology will not only augment diagnostic capabilities but also redefine the future of autonomous medical imaging.



## References

- [1] Wang, X., Peng, Y., Le, L., Lu, Z., Bagheri, M., & Summers, R. M. (2017). ChestX-Ray8: Hospital-Scale Chest X-Ray Database and Benchmarks on Weakly-Supervised Classification and Localization of Common Thorax Diseases. 3462–3471. <https://doi.org/10.1109/cvpr.2017.369>
- [2] Prevedello, L. M., Erdal, B. S., Ryu, J. L., Little, K. J., Demirer, M., Qian, S., & White, R. D. (2017). Automated Critical Test Findings Identification and Online Notification System Using Artificial Intelligence in Imaging. *Radiology*, 285(3), 923–931. <https://doi.org/10.1148/RADIOL.2017162664>
- [3] Candemir, S., Jaeger, S., Palaniappan, K., Musco, J. P., Singh, R., Xue, Z., Karargyris, A., Antani, S., Thoma, G. R., & McDonald, C. J. (2014). Lung Segmentation in Chest Radiographs Using Anatomical Atlases With Nonrigid Registration. *IEEE Transactions on Medical Imaging*, 33(2), 577–590. <https://doi.org/10.1109/TMI.2013.2290491>
- [4] Almeida, H., Jean-Louis, L., & Meurs, M.-J. (2017). Retrieving biomedical literature: an open source search engine based on open access resources. *F1000Research*, 6. <https://doi.org/10.7490/F1000RESEARCH.1113636.1>
- [5] Esteva, A., Robicquet, A., Ramsundar, B., Kuleshov, V., DePristo, M. A., Chou, K., Cui, C., Corrado, G. S., Thrun, S., & Dean, J. (2019). A guide to deep learning in healthcare. *Nature Medicine*, 25(1), 24–29. <https://doi.org/10.1038/S41591-018-0316-Z>
- [6] Lundervold, A., & Lundervold, A. (2019). An overview of deep learning in medical imaging focusing on MRI. *Zeitschrift Fur Medizinische Physik*, 29(2), 102–127. <https://doi.org/10.1016/J.ZEMEDI.2018.11.002>
- [7] Jalloul, M., Alkhulaifat, D., Miranda-Schaeubinger, M., De Leon Benedetti, L., Otero, H. J., & Dako, F. (2024). Artificial Intelligence in Chest Radiology: Advancements and Applications for Improved Global Health Outcomes. *Current Pulmonology Reports*. <https://doi.org/10.1007/s13665-023-00334-9>
- [8] Olawade, D. B., Wada, O. J., David-Olawade, A. C., Kunonga, E., Abaire, O. J., & Ling, J. (2023). Using artificial intelligence to improve public health: a narrative review. *Frontiers in Public Health*. <https://doi.org/10.3389/fpubh.2023.1196397>
- [9] Tang, Y., Tang, Y., Peng, Y., Yan, K., Bagheri, M., Redd, B., Brandon, C., Lu, Z., Han, M., Xiao, J., & Summers, R. M. (2020). Automated abnormality classification of chest radiographs using deep convolutional neural networks. 3(1), 70. <https://doi.org/10.1038/S41746-020-0273-Z>
- [10] Ronneberger, O., Fischer, P., & Brox, T. (2015). U-Net: Convolutional Networks for Biomedical Image Segmentation. *Lecture Notes in Computer Science*, 234–241. [https://www.academia.edu/52644638/U\\_Net\\_Convolutional\\_Networks\\_for\\_Biomedical\\_Image\\_Segmentation](https://www.academia.edu/52644638/U_Net_Convolutional_Networks_for_Biomedical_Image_Segmentation)

- [11] Firdiantika, I. M., & Jusman, Y. (2022). Pneumonia detection in chest X-ray images using convolutional neural network. *Nucleation and Atmospheric Aerosols*. <https://doi.org/10.1063/5.0105004>
- [12] Ahmed, Z., Wan, S., Zhang, F., & Zhong, W. (2024). Artificial intelligence for omics data analysis. <https://doi.org/10.1186/s44330-024-00004-5>
- [13] Nam, J. G., Park, S., Hwang, E. J., Lee, J. H., Jin, K. N., Lim, K. Y., Vu, T. H., Sohn, J. H., Hwang, S., Goo, J. M., & Park, C. M. (2019). Development and Validation of Deep Learning-based Automatic Detection Algorithm for Malignant Pulmonary Nodules on Chest Radiographs. *Radiology*, *290*(1), 218–228. <https://doi.org/10.1148/RADIOL.2018180237>
- [14] Albertini, D. A., Carminati, B., & Ferrari, E. (2017). An extended access control mechanism exploiting data dependencies. *International Journal of Information Security*, *16*(1), 75–89. <https://doi.org/10.1007/S10207-016-0322-4>
- [15] Allaouzi, I., & Ben Ahmed, M. (2019). A Novel Approach for Multi-Label Chest X-Ray Classification of Common Thorax Diseases. *IEEE Access*, *7*, 64279–64288. <https://doi.org/10.1109/ACCESS.2019.2916849>
- [16] Wang, H., Du, H., Zhao, Y., & Yan, J. (2020). A Comprehensive Overview of Person Re-Identification Approaches. *IEEE Access*, *8*, 45556–45583. <https://doi.org/10.1109/ACCESS.2020.2978344>
- [17] Litjens, G., Kooi, T., Ehteshami Bejnordi, B., Setio, A. A. A., Ciompi, F., Ghafoorian, M., van der Laak, J., van Ginneken, B., & Sánchez, C. I. (2017). A survey on deep learning in medical image analysis. *Medical Image Analysis*, *42*, 60–88. <https://doi.org/10.1016/J.MEDIA.2017.07.005>
- [18] overleaf Sheng, B., Xiang, D., & Ye, P. (2015). Convergence rate of semi-supervised gradient learning algorithms. *International Journal of Wavelets, Multiresolution and Information Processing*, *13*(04), 1550021. <https://doi.org/10.1142/S0219691315500216>
- [19] Tahmoresnezhad, J., & Hashemi, S. (2016). Transductive transfer learning via maximum margin criterion. *Scientia Iranica*, *23*(3), 1239–1250. <https://doi.org/10.24200/SCI.2016.3892>
- [20] Frid-Adar, M., Diamant, I., Klang, E., Amitai, M., Goldberger, J., & Greenspan, H. (2018). GAN-based synthetic medical image augmentation for increased CNN performance in liver lesion classification. *Neurocomputing*, *321*, 321–331. <https://doi.org/10.1016/J.NEUCOM.2018.09.013>
- [21] Wu, X., Feng, Y., Xu, H., Lin, Z., Chen, T., Li, S., Qiu, S., Liu, Q., Ma, Y., & Zhang, S. (2023). CTransCNN: Combining transformer and CNN in multilabel medical image classification. *Knowledge Based Systems*. <https://doi.org/10.1016/j.knosys.2023.111030>

- [22] Castiglioni, I., Rundo, L., Codari, M., Di Leo, G., Salvatore, C., Interlenghi, M., Galivanone, F., Cozzi, A., D'Amico, N. C., & Sardanelli, F. (2021). AI applications to medical images: From machine learning to deep learning. *Physica Medica*, *83*, 9–24. <https://doi.org/10.1016/J.EJMP.2021.02.006>
- [23] Schlemper, J., Oktay, O., Schaap, M., Heinrich, M. P., Kainz, B., Glocker, B., & Rueckert, D. (2019). Attention gated networks: Learning to leverage salient regions in medical images. *Medical Image Analysis*, *53*, 197–207. <https://doi.org/10.1016/J.MEDIA.2019.01.012>
- [24] Lee, S. M., Seo, J. B., Yun, J., Cho, Y.-H., Vogel-Claussen, J., Schiebler, M. L., Gefter, W. B., van Beek, E. J. R., Goo, J. M., Lee, K. S., Hatabu, H., Gee, J. C., & Kim, N. (2019). Deep Learning Applications in Chest Radiography and Computed Tomography: Current State of the Art. *Journal of Thoracic Imaging*, *34*(2), 75–85. <https://doi.org/10.1097/RTI.0000000000000387>